LETTER

doi:10.1038/nature25484

# Probing the interatomic potential of solids with strong-field nonlinear phononics

A. von Hoegen[1], R. Mankowsky[1], M. Fechner[1], M. Först[1] & A. Cavalleri[1,2]

**Nonlinear optical techniques at visible frequencies have long been applied to condensed matter spectroscopy[1]. However, because many important excitations of solids are found at low energies, much can be gained from the extension of nonlinear optics to mid-infrared and terahertz frequencies[2,3]. For example, the nonlinear excitation of lattice vibrations has enabled the dynamic control of material functions[4–8]. So far it has only been possible to exploit second-order phonon nonlinearities[9] at terahertz field strengths near one million volts per centimetre. Here we achieve an order-of-magnitude increase in field strength and explore higher-order phonon nonlinearities. We excite up to five harmonics of the $A_1$ (transverse optical) phonon mode in the ferroelectric material lithium niobate. By using ultrashort mid-infrared laser pulses to drive the atoms far from their equilibrium positions, and measuring the large-amplitude atomic trajectories, we can sample the interatomic potential of lithium niobate, providing a benchmark for *ab initio* calculations for the material. Tomography of the energy surface by high-order nonlinear phononics could benefit many aspects of materials research, including the study of classical and quantum phase transitions.**

In the experiments reported here, the highest-frequency $A_1$ mode of $LiNbO_3$ was excited with mid-infrared femtosecond pulses tuned to 17.5 THz, immediately to the red of the transverse-optical phonon frequency ($\nu_{TO} = 19$ THz)[10,11]. In the linear response regime, the real-space distortions of this mode involve rotations of the oxygen octahedra, accompanied by *c*-axis motions against the niobium and lithium sublattices (see Fig. 1a). Owing to the broken inversion symmetry of the crystal, the $A_1$ mode is both Raman- and infrared-active[10,11], with electric dipole moment along the *c* axis. Here, we explore the response of this mode up to very high amplitudes.

To study the dynamics of the driven mode, we measured time-dependent polarization rotation and second-harmonic intensity using 30-fs-long probe pulses at a wavelength of 800 nm. The polarization rotation yielded changes in the dielectric permittivity of the crystal $\varepsilon_r(\tau)$, whereas the second harmonic sampled the changes in the optical second-order susceptibility $\chi^{(2)}(\tau)$ (refs 12, 13) and with it the polar component of the lattice motion. Crucially, the stable absolute carrier-envelope phase (CEP)[14] of the pump field (Fig. 1b) made it possible to follow the atomic trajectories directly. Spectral interferometry between the polarization rotation and second-harmonic signals and their respective local oscillators derived from the same probe pulses yielded both the phase and the amplitude of these dynamics. The time resolution of these experiments was dictated by the bandwidths of the local oscillators on the detector[15,16], 60 THz and 80 THz for the second harmonic and polarization rotation, respectively. Hence, the measurements were sensitive to the phase of the signal oscillations up to the fifth overtone of the excited transverse-optical phonon mode (see Methods and Extended Data Figs 1–3 for details).

For small-amplitude excitation (0.1 MV cm$^{-1}$), both polarization rotation and second-harmonic measurements yielded harmonic oscillations (see Fig. 1c, d, dashed lines), which were readily attributed to a combination of a 15 THz phonon-polariton and the 19 THz transverse-optical phonon of the $A_1$ mode[17]. As shown in Methods (Extended Data Fig. 4), the pump–probe spectrum of the small-field response is well understood by considering the

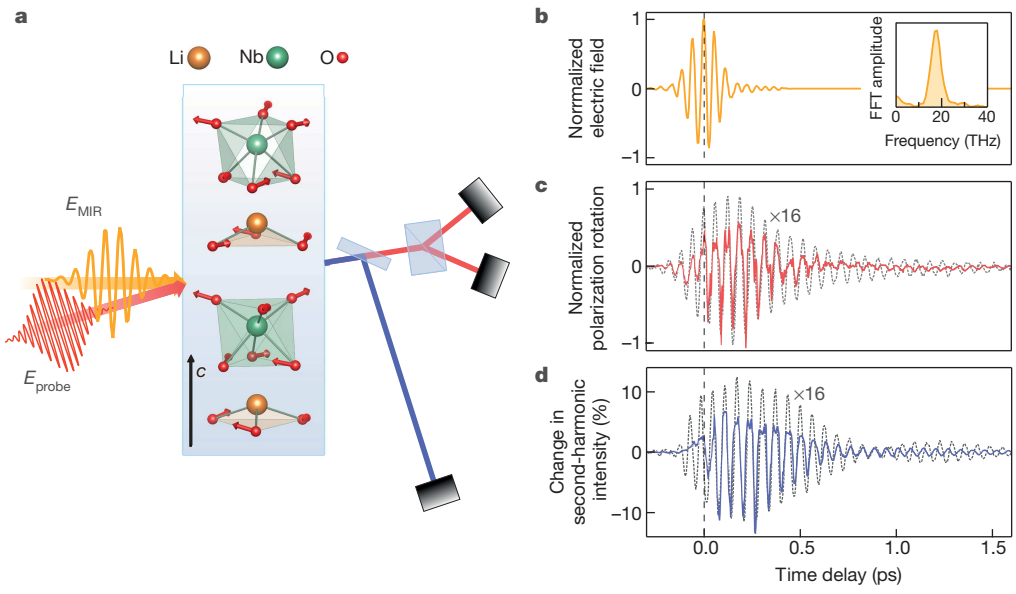


**Figure 1 | Experimental set-up and time-resolved optical response.** **a**, Schematic of the pump–probe geometry. The resonantly excited $A_1$ phonon mode in $LiNbO_3$ is also shown with a polar component along the crystal *c* axis. **b**, Electro-optic sampling measurement of the CEP-stable pump pulses, which are 150 fs long, centred at 17.5 THz with 4 THz bandwidth. **c**, **d**, Time-resolved polarization rotation of the 800 nm probe (**c**) and changes in the second-harmonic intensity (**d**), for high (solid lines) and low (dashed lines) excitation fields. FFT, fast Fourier transform; MIR, mid-infrared.

[1]Max Planck Institute for the Structure and Dynamics of Matter, 22761 Hamburg, Germany. [2]Department of Physics, University of Oxford, Clarendon Laboratory, Oxford OX1 3PU, UK.

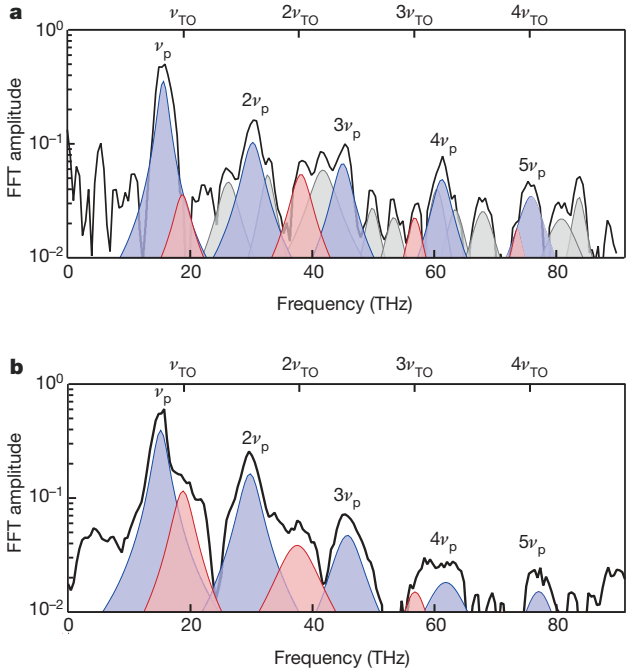


**Figure 2 | Spectra of time-resolved optical responses and harmonic field dependences.** **a**, **b**, FFT amplitude spectra of the polarization rotation (**a**) and second-harmonic intensity (**b**) measurements, for the high excitation field shown in Fig. 1. The blue peaks and red peaks correspond to multiples of the phonon-polariton frequencies $\nu_p$ (15.3 THz at 800 nm, 16.2 THz at 400 nm) and $\nu_{TO}$, respectively. The grey peaks in **a** label sum and difference frequencies of $\nu_p$ and $\nu_{TO}$, which are absent in the second-harmonic response. **c**, Excitation field dependence of the peak area at the first, second and third harmonic of $\nu_p$, revealing a linear, quadratic and cubic dependence. Error bars represent the standard deviation $\sigma$ calculated from the noise level of the experiment.

phase-matching between the probe light and the phonon-polariton propagating into the crystal[18,19].

At high pump fields (20 MV cm$^{-1}$, Fig. 1c, d, solid lines), a strongly anharmonic response was observed, with asymmetric oscillations in both polarization rotation and second-harmonic signals. The corresponding amplitude spectra are shown in Fig. 2a, b. In addition to the fundamental frequency components, several harmonics appeared. The most pronounced peaks were found at multiples of the 15 THz phonon-polariton mode, visible up to $n = 5$ (75 THz). Correspondingly, the amplitudes of the first three harmonics at $\nu = 15$ THz, 30 THz and 45 THz displayed a linear, quadratic and cubic dependence on the excitation field (see Fig. 2c). The polarization rotation spectrum also exhibited peaks at the sum and difference frequencies of these harmonics (see Extended Data Fig. 5 for detailed assignments of all peaks). These data are reminiscent of what has been extensively reported in the literature in the context of non-resonant terahertz and mid-infrared harmonic generation[20–25]. Here, however, the harmonics appear at multiples of the phonon-polariton frequency, instead of the central frequency of the optical pump field, indicating a different physical origin.

To analyse these data, we first consider the local lattice response. We start from the anharmonic lattice potential of the driven mode at $\omega_{TO}$ and ignore phonon-polariton propagation. *Ab initio* density functional theory (DFT) calculations (see Methods) yield the anharmonic lattice potential plotted in Fig. 3. This potential can be fitted by

$$U(Q_{IR}) = \frac{1}{2}\omega_{TO}^2 Q_{IR}^2 + \frac{1}{3}a_3 Q_{IR}^3 + \frac{1}{4}a_4 Q_{IR}^4 + \frac{1}{5}a_5 Q_{IR}^5 \qquad (1)$$

where $Q_{IR}$ denotes the amplitude of the infrared-active mode, $\omega_{TO} = 2\pi\nu_{TO}$, and $a_3$, $a_4$ and $a_5$ are the coefficients of the cubic, quartic and quintic potential terms. Note that, in the potential of equation (1), we have omitted all terms that describe the coupling to other vibrational modes $Q_j$ of the form $\sum_j Q_{IR}^2 Q_j$ (refs 5, 8, 9). These terms displace the average lattice structure along all the coupled coordinates $Q_j$ and renormalize the eigenfrequency of the driven mode $Q_{IR}$. However, as shown in Extended Data Fig. 6, the effect is small and will not be discussed here.

Starting from the potential energy of equation (1), we derive the equation of motion for $Q_{IR}$, considering excitation with a mid-infrared light pulse of carrier frequency $\omega_{MIR}$ and duration $T$

$$\ddot{Q}_{IR} + 2\gamma\dot{Q}_{IR} + \omega_{TO}^2 Q_{IR} + a_3 Q_{IR}^2 + a_4 Q_{IR}^3 + a_5 Q_{IR}^4 = Z^* E(t) \qquad (2)$$

Here, $Z^*$ denotes the effective charge of the phonon mode, $\gamma$ is a dissipation constant, and $E(t) = E_0 \sin(\omega_{MIR} t)\exp(-t^2/T^2)$ is the excitation pulse profile. The calculated dynamics at the field strengths of 20 MV cm$^{-1}$ used in the experiment are reported in Fig. 3 and predict peaks at harmonics of the fundamental frequency $\nu_{TO}$.

A more comprehensive description of our experimental observations was obtained when propagation effects were taken into account. Finite-difference time-domain (FDTD)[26] simulations of phonon-polariton

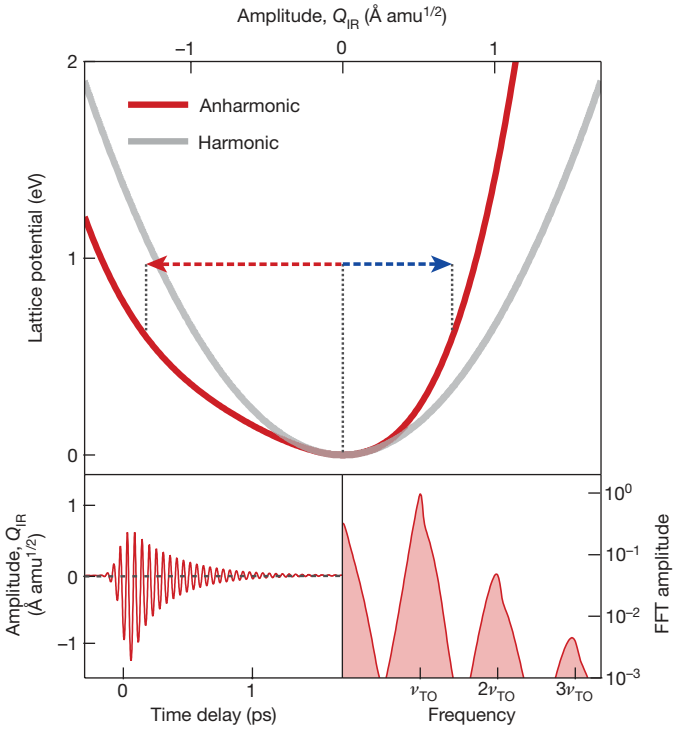


**Figure 3 | Calculated $A_1$-mode potential energy.** The calculated lattice potential energy of $LiNbO_3$ (red) of the $A_1$ mode shown in Fig. 1a is compared to a harmonic potential (grey) with the same fundamental frequency $\omega_{TO}$. The arrows denote the expected positive and negative excursions for an energy of 0.6 eV, corresponding to the energy deposited per unit cell by the excitation pulses. The lower plots show the solution of the equation of motion and its amplitude spectrum.

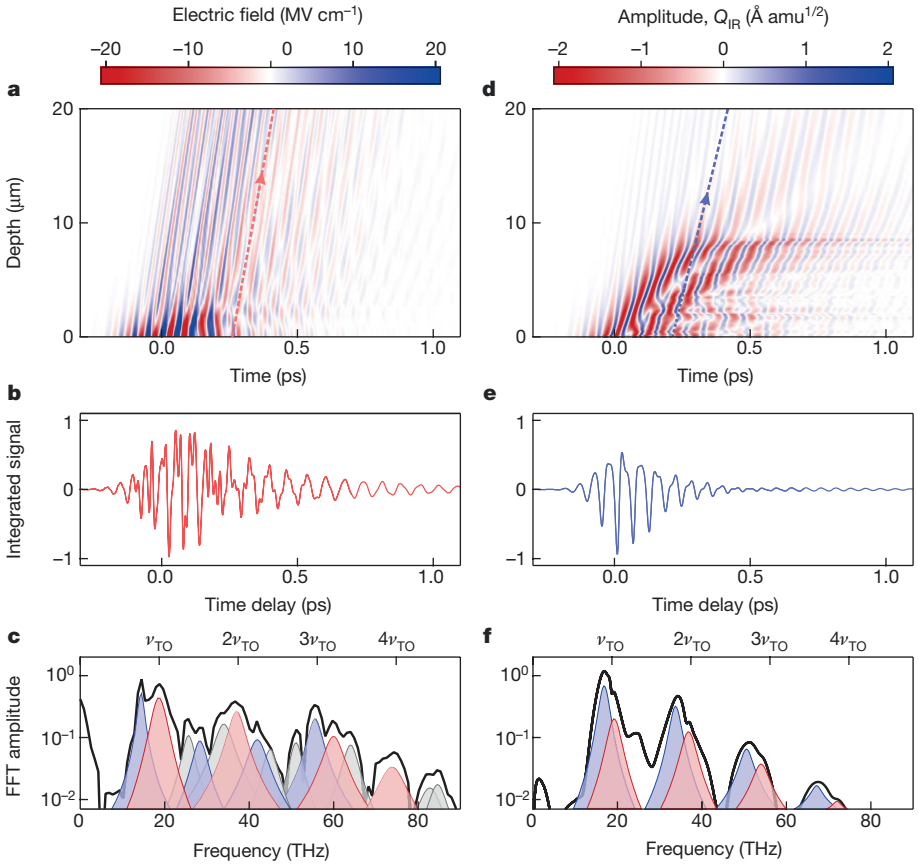


**Figure 4 | FDTD simulations for the phonon-polariton propagation. a**, Contour plot of the electric field as a function of depth $d$ and time $t$ inside $LiNbO_3$ after mid-infrared excitation. The red dashed line shows the propagation of the 800 nm probe pulse for one pump–probe time delay $\tau$, following the relation $d_{800} = v_g t$. **b**, **c**, Time trace derived by integrating along the dashed red line in **a** for all pump–probe delays (**b**), and the corresponding amplitude spectrum (**c**). The spectrum shows harmonics of $\nu_p$ and $\nu_{TO}$ as well as mixed frequencies. **d**, Contour plot of the vibrational amplitude $Q_{IR}$ after the same mid-infrared excitation as in **a**. The dashed blue line shows the propagation of the second-harmonic light at 400 nm, also for a single time delay $\tau$. **e**, Time trace derived by spatially integrating the time derivative of $Q_{IR}$ along the dashed blue line within the first 2 μm for all pump–probe delays. **f**, Amplitude spectrum of **e**, which shows broad peaks only at the harmonics of $\nu_p$ and $\nu_{TO}$.

propagation are reported in Fig. 4. In these simulations, we combined the linear optical properties of $LiNbO_3$ (Extended Data Table 1) with the nonlinear lattice potential of equation (1) (see Methods and Extended Data Fig. 7). Figure 4a displays the amplitude of the propagating electric field as a function of sample depth $d$ and time $t$. Both the phonon-polaritons and the broadband radiation emitted from the anharmonic motions propagate from the surface into the bulk, following the dispersion imposed by the material. By integrating the simulated electric field along the 800 nm light line, $d_{800} = v_g t$ (red dashed line in Fig. 4a, with $v_g$ the group velocity), for each pump–probe time delay $\tau$, we extracted the response shown in Fig. 4b, yielding good qualitative agreement with the polarization rotation measurement (compare Figs 4b and 1c). Figure 4c displays the corresponding amplitude spectrum, which comprises peaks at all sum and difference frequencies of the polariton and the transverse-optical mode, also in good agreement with experiment (see Fig. 2a).

We next turn to the key results of this paper, which are extracted from the time-dependent changes in the second-harmonic intensity $I_{SH}(\tau)$. As discussed elsewhere[12,13,27], a coherent phonon of frequency $\Omega$ generates frequency-shifted radiation in the second-harmonic field $E_{SH}$ because of hyper-Raman scattering. Crucially, the detected spectral interferometry signal is proportional to the lattice velocity, $I_{SH}(\tau) = B\dot{Q}(\tau)$ (see also Methods and refs 27, 28). Therefore, we can compare the simulations of Fig. 4e, f with the experiments of Figs 1d and 2b by spatially integrating the time derivative of the simulated lattice coordinate $Q(t, z)$ along the 400 nm light line (Fig. 4d, dashed blue line). This integral was taken over the first 2 μm beneath the surface, where the second-harmonic light is generated in the experiment[8]. The corresponding simulated signal $I_{SH}(\tau)$ (Fig. 4e) contains frequency components at multiples of 16 THz and 19 THz (see Fig. 4f), in agreement with the measured data of Fig. 2b.

Most importantly, from the knowledge of $\dot{Q}(\tau)$, the microscopic lattice potential $U(Q)$ explored during each oscillation cycle could be reconstructed. We consider the coherent dynamics of the lattice at times after the pump pulse, that is, when no force is being applied onto the mode. For weak phonon damping ($\gamma \ll \Omega$), the total energy of the unforced oscillating lattice can be approximated as being constant over each cycle, $U(\tau) + E_{kin}(\tau) = \varepsilon$. Hence, we could retrieve the instantaneous potential energy $U(\tau) = \varepsilon - E_{kin}(\tau)$ from the knowledge of the kinetic energy, which is in turn proportional to the square of the measured second-harmonic signal $E_{kin}(\tau) = \frac{1}{2}\dot{Q}(\tau)^2 = \frac{1}{2}I_{SH}(\tau)^2/B^2$. The instantaneous potential energy $U(\tau)$, which was known except for a proportionality term $1/B^2$, could then be converted into $U(Q)$ by a time integral of the second-harmonic signal $I_{SH}(\tau) = B\dot{Q}(\tau)$, which yielded $Q(\tau)$. Hence, we could extract the shape of the lattice potential apart from a single proportionality constant. Because different cycles with different amplitudes and different total energy $\varepsilon$ trace fractions of the potential energy $U(Q)$ many times, the shape of the potential reconstructed in this way was highly over-determined.

Figure 5 compares the lattice potential of the $A_1$ mode calculated from DFT (grey line) to the reconstructed potential (filled circles). The calculated and reconstructed curves were matched by adjusting one free parameter $B$ (see Methods for details). Within the systematic uncertainties of DFT calculations (light grey shaded area), we find agreement between the shapes of the anharmonic potentials up to the highest amplitudes reached experimentally.

The tomography of the force field discussed above is straightforwardly extensible to all materials with a large bandgap, such as ferroelectrics, for which acceleration of quasiparticles in the field is neglected to first order. We note that direct measurements of the coordinate $Q(\tau)$ with femtosecond X-ray diffraction, for example from a free electron laser with pulses that are appropriately synchronized with the absolute phase of a strong terahertz field, would allow an unbiased measurement of the potential, without the need for comparing the data to a calculated potential and determining the constant. Also, full reconstruction of the force field of a material with $N$ atoms

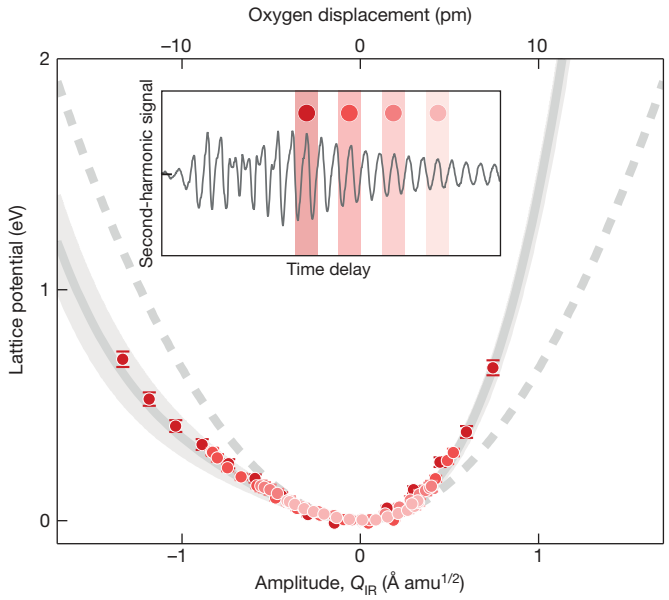


**Figure 5 | Reconstructed $A_1$-mode potential energy.** The potential energy of the $A_1$ mode (red filled circles) was reconstructed from different cycles of the time-resolved second-harmonic measurement shown in the inset. Error bars represent the standard deviation $\sigma$ calculated from the noise level of the experiment. The grey solid line is the mode potential obtained by DFT calculations, and the light grey shaded area is an estimate of its systematic uncertainties. The experimental potential is scaled to the calculated potential using a single scaling factor (see Methods). From this comparison, we estimate maximum mode excursions of 1.4 Å amu$^{1/2}$ (where amu is atomic mass unit), corresponding to displacements of the oxygen atoms by about 14 picometres from their equilibrium positions. The dashed grey curve is the potential in the harmonic approximation.

requires the measurement of $3N-3$ lattice modes without symmetry considerations. Recent advances in the generation of mid-infrared and terahertz pulses that are both widely tunable and intense[29] make these prospects realistic. Tomographic measurements of force potentials in the vicinity of equilibrium phase transitions will yield crucial information not accessible otherwise. Finally, as the sampling of the potential can be retrieved within one cycle of the pump light, we envisage measurements of rapidly evolving potential energy surfaces.

**Online Content** Methods, along with any additional Extended Data display items and Source Data, are available in the online version of the paper; references unique to these sections appear only in the online paper.

**Received 27 June; accepted 4 December 2017.**
**Published online 21 February 2018.**

1. Shen, Y. R. *The Principles of Nonlinear Optics* (Wiley-Interscience, 2002).
2. Kampfrath, T., Tanaka, K. & Nelson, K. A. Resonant and nonresonant control over matter and light by intense terahertz transients. *Nat. Photon.* **7,** 680–690 (2013).
3. Nicoletti, D. & Cavalleri, A. Nonlinear light–matter interaction at terahertz frequencies. *Adv. Opt. Photonics* **8,** 401–464 (2016).
4. Mitrano, M. *et al.* Possible light-induced superconductivity in $K_3C_{60}$ at high temperature. *Nature* **530,** 461–464 (2016).
5. Mankowsky, R. *et al.* Nonlinear lattice dynamics as a basis for enhanced superconductivity in $YBa_2Cu_3O_{6.5}$. *Nature* **516,** 71–73 (2014).
6. Nova, T. F. *et al.* An effective magnetic field from optically driven phonons. *Nat. Phys.* **13,** 132–136 (2017).
7. Fausti, D. *et al.* Light induced superconductivity in a stripe-ordered cuprate. *Science* **331,** 189–191 (2011).
8. Mankowsky, R., von Hoegen, A., Först, M. & Cavalleri, A. Ultrafast reversal of the ferroelectric polarization. *Phys. Rev. Lett.* **18,** 197601 (2017).
9. Först, M. *et al.* Nonlinear phononics as a new ultrafast route to lattice control. *Nat. Phys.* **7,** 854–856 (2011).
10. Schaufele, R. F. & Weber, M. J. Raman scattering by lithium niobate. *Phys. Rev.* **152,** 705–708 (1966).
11. Barker, A. S. & Loudon, R. Dielectric properties and optical phonons in $LiNbO_3$. *Phys. Rev.* **158,** 433–445 (1967).
12. Chang, Y.-M., Xu, L. & Tom, H. W. K. Observation of local-interfacial optical phonons at buried interfaces using time-resolved second-harmonic generation. *Phys. Rev. B* **59,** 12220–12223 (1999).
13. Denisov, V. N., Mavrin, B. N. & Podobedov, V. B. Hyper-Raman by vibrational excitations in crystals, glasses and liquids. *Phys. Rep.* **151,** 1–92 (1987).
14. Sell, A., Leitenstorfer, A. & Huber, R. Phase-locked generation and field-resolved detection of widely tunable terahertz pulses with amplitudes exceeding 100 MV/cm. *Opt. Lett.* **33,** 2767–2769 (2008).
15. Keiber, S. *et al.* Electro-optic sampling of near-infrared waveforms. *Nat. Photon.* **10,** 159–162 (2016).
16. Porer, M., Ménard, J.-M. & Huber, R. Shot noise reduced terahertz detection via spectrally postfiltered electro-optic sampling. *Opt. Lett.* **39,** 2435–2438 (2014).
17. Kojima, S., Kanehara, K., Hoshina, T. & Tsurumi, T. Optical phonons and polariton dispersions of congruent $LiNbO_3$ studied by far-infrared spectroscopic ellipsometry and Raman scattering. *Jpn. J. Appl. Phys.* **55,** 10TC02 (2016).
18. Claus, R. Light scattering by optical phonons and polaritons in perfect crystals. *Phys. Status Solidi B* **50,** 11–32 (1972).
19. Dastrup, B. S., Hall, J. R. & Johnson, J. A. Experimental determination of the interatomic potential in $LiNbO_3$ via ultrafast lattice control. *Appl. Phys. Lett.* **110,** 162901 (2017).
20. Ghimire, S. *et al.* Observation of high-order harmonic generation in a bulk crystal. *Nat. Phys.* **7,** 138–141 (2011).
21. Schubert, O. *et al.* Sub-cycle control of terahertz high-harmonic generation by dynamical Bloch oscillations. *Nat. Photon.* **8,** 119–123 (2014).
22. Zaks, B., Liu, R. B. & Sherwin, M. S. Experimental observation of electron–hole recollisions. *Nature* **483,** 580–583 (2012).
23. Vampa, G. *et al.* Linking high harmonics from gases and solids. *Nature* **522,** 462–464 (2015).
24. Itatani, J. *et al.* Tomographic imaging of molecular orbitals. *Nature* **432,** 867–871 (2004).
25. Langer, F. *et al.* Lightwave-driven quasiparticle collisions on a subcycle timescale. *Nature* **533,** 225–229 (2016).
26. Taflov, A. & Hagness, S. C. *Computational Electrodynamics: The Finite-Difference Time-Domain Method* (Artech House, 2000).
27. Yan, Y. X., Gamble, E. B. Jr & Nelson, K. A. Impulsive stimulated scattering: General importance in femtosecond laser pulse interactions with matter, and spectroscopic applications. *J. Chem. Phys.* **83,** 5391–5399 (1985).
28. Merlin, R. Generating coherent THz phonons with light pulses. *Solid State Commun.* **102,** 207–220 (1997).
29. Liu, B. *et al.* Generation of narrowband, high-intensity, carrier-envelope phase stable pulses tunable between 4 and 18 THz. *Opt. Lett.* **42,** 129–131 (2017).

**Acknowledgements** We thank R. Merlin and M. Altarelli for discussions. The research leading to these results received funding from the European Research Council under the European Union's Seventh Framework Programme (FP7/2007–2013)/ERC Grant Agreement No. 319286 (QMAC). We acknowledge support from the Deutsche Forschungsgemeinschaft via the excellence cluster 'The Hamburg Centre for Ultrafast Imaging—Structure, Dynamics and Control of Matter at the Atomic Scale' and the Priority Program SFB925 'Light induced Dynamics and Control of Correlated Quantum Systems'.

**Author Contributions** A.C., together with A.v.H. and R.M., conceived this project. R.M., A.v.H. and M. Först built the experimental set-up. A.v.H. and R.M. conducted the experiment and analysed the data. M. Fechner performed the DFT calculations. A.v.H. conducted the FDTD simulation. All authors interpreted the data and contributed to the manuscript.

**Author Information** Reprints and permissions information is available at www.nature.com/reprints. The authors declare no competing financial interests. Readers are welcome to comment on the online version of the paper. Publisher's note: Springer Nature remains neutral with regard to jurisdictional claims in published maps and institutional affiliations. Correspondence and requests for materials should be addressed to A.A. (andrea.cavalleri@mpsd.mpg.de) or A.v.H. (alexander.von-hoegen@mpsd.mpg.de).

**Reviewer Information** *Nature* thanks M. Kira and the other anonymous reviewer(s) for their contribution to the peer review of this work.

## METHODS

**Experimental set-up.** The CEP-stable, 150-fs-long, 17.5 THz mid-infrared pump pulses of 4 THz bandwidth were obtained by mixing the two signal beams from two optical parametric amplifiers, which were seeded by the same white light and pumped by 30 fs, 800 nm pulses at a repetition rate of 1 kHz. The nonlinear lattice dynamics in $LiNbO_3$ were probed by a time-delayed replica of the 800 nm pulses, in non-collinear geometry with an angle of 30° to the mid-infrared pump (see Extended Data Fig. 1). The CEP stability of the excitation pulse is reflected in phase stability of the resonantly driven coherent oscillations of the $A_1$ phonon mode.

The pump-induced polarization rotation (PR) of the 800 nm beam was measured by detecting the time-resolved difference signal of two intensity-balanced photodiodes placed behind a half-wave plate and a Wollaston prism.

Owing to the large second-order nonlinear susceptibility of $LiNbO_3$, the 800 nm probe pulses also generated second-harmonic (SH) light at 400 nm, which was separated from the fundamental beam after the sample by a dichroic mirror and detected with a photomultiplier tube. The SH signal originates from a layer of one coherence length $l_c = 1.3\,\mu m$ below the surface[8,30].

All experiments were conducted at room temperature. The sample used in the experiments was a commercially available congruent $LiNbO_3$ single crystal (5 mm × 5 mm × 5 mm).

**PR and SH detection processes.** The nonlinear interaction of a lattice vibrational mode with an optical probe pulse involves Raman scattering in PR measurements and hyper-Raman scattering in SH measurements[12,13,27,28]. These processes can be described by the wave equation

$$\frac{\partial^2 E}{\partial z^2} - \frac{n^2}{c^2}\frac{\partial^2 E}{\partial t^2} = \rho\frac{\partial^2 (E_{\mathrm{probe}} Q)}{\partial t^2}$$

where $n$ is the refractive index of the material and $c$ the vacuum speed of light. The constant $\rho$ contains the number density of oscillators and the Raman cross-section. $E_{\mathrm{probe}}$ denotes the probe laser field at angular frequency $\omega_{\mathrm{probe}}$ (refs 27, 28), that is, the fundamental 800 nm light in the PR measurement and the 400 nm light in the SH measurement. $Q(z, t+\tau) = Q_0(z)\sin[\Omega(t+\tau)]$ is the time-dependent amplitude of the excited vibrational mode, with $\tau$ the time delay between pump and probe pulses. A general solution to this equation is[27,28]

$$E(z,t) = E_{\mathrm{probe}}(z,t) - a\frac{\partial}{\partial t}(Q(z, t+\tau)E_{\mathrm{probe}}(z,t))$$

showing that the probe electric field is modulated by the time derivative of $Q(z, t+\tau)E_{\mathrm{probe}}(z,t)$. After interaction with a phonon-polariton of frequency $\Omega$ and at a specific time delay, the spectrum of the transmitted probe, which is the Fourier transform of $E(z,t)$, reads

$$E(\omega) = E_{\mathrm{probe}}(\omega) + \beta\omega[E_{\mathrm{probe}}(\omega+\Omega)\exp(i\Omega\tau) - E_{\mathrm{probe}}(\omega-\Omega)\exp(-i\Omega\tau)]$$

It contains the unperturbed probe spectrum $E_{\mathrm{probe}}(\omega)$ and sidebands generated at $\omega_{\mathrm{probe}} \pm \Omega$. Importantly, these sidebands acquire a time-delay-dependent phase $\exp(\pm i\Omega\tau)$. Their phase-sensitive detection, for example achieved by spectral interference with the local oscillator $E_{\mathrm{probe}}(\omega)$ on the detector, carries information about both phase and amplitude of the phonon-polariton[15,16].

In this case, the measured intensity at a time delay $\tau$ is

$$\begin{aligned} I(\tau) &= \int \mathrm{d}\omega\{|E_{\mathrm{probe}}(\omega) + \beta\omega[E_{\mathrm{probe}}(\omega+\Omega)\exp(i\Omega\tau) \\ &\quad - E_{\mathrm{probe}}(\omega-\Omega)\exp(-i\Omega\tau)]|^2\} \\ &= I_{\mathrm{probe}} + \alpha\Omega\cos(\Omega\tau) + \gamma\Omega^2\cos(2\Omega\tau) \end{aligned}$$

We disregard the homodyne component proportional to $\gamma\Omega^2$, which is far smaller than the heterodyne component, proportional to $\alpha\Omega$ (ref. 32). Hence, the detected interference signal is[27,28,31]

$$I(\tau) = I_{\mathrm{probe}} + \alpha\Omega\cos(\Omega\tau)$$

Crucially, this time-delay-dependent signal is phase-shifted by $\pi/2$ and amplitude scaled proportional to $\Omega$ with respect to the lattice vibration $Q(t) = Q_0\sin[\Omega(t+\tau)]$. Hence, it is proportional to the velocity of the vibrational motion $\dot{Q}(\tau)$. For in-depth discussion, we refer to refs 27, 28 and 31.

In the PR measurements, the detected difference signal is $\Delta I(\tau) = I_{\parallel}(\tau) - I_{\perp}(\tau) = 2\alpha\Omega\cos(\Omega\tau)$

The time resolution is determined by the bandwidth of the local oscillator at the detector[15,16] which is spectrally broadened with respect to the incident pulse owing to self-phase modulation in the $LiNbO_3$ crystal[32,33] (see Extended Data Fig. 3a). The sampling efficiency, calculated according to ref. 15 and shown in Extended Data Fig. 3b, allows efficient detection up to 80 THz. Further, the interaction length between the 800 nm probe and the phonon-polariton harmonics is determined by the penetration depths, which increase with increasing harmonic order (see also Extended Data Fig. 3b). As result, the PR measurements cannot be used to quantify the amplitude of the atomic motions in a straightforward manner.

In the SH measurement, the detected light is generated in a thin layer extending to 1.3 μm below the sample surface[8,30]. Therefore, the interaction length with the phonon-polariton harmonics does not change for different harmonic orders. The SH bandwidth supports efficient detection up to 60 THz (see Extended Data Fig. 3c, d). A bandpass filter was used to shape the spectral response function in order to flatten the sampling efficiency for the first three harmonics[15,31].

The phonon-polariton induced oscillatory signal components were extracted from the $I_{\mathrm{SH}}(\tau)$ data via subtraction of a slowly varying background, which results from the modification of $\chi^{(2)}$ due to changes in the ferroelectric polarization (see ref. 8).

**Phase-matching between probe light and phonon-polariton.** The amplitude spectra shown in Extended Data Fig. 4 are well understood by considering the phase-matching between the probe light and the phonon-polariton propagating into the crystal. The phonon-polariton dispersion of $LiNbO_3$ is plotted as $\nu_{\mathrm{p}} = \frac{c_0}{\sqrt{\varepsilon(\nu)}}q$, where $c_0$ is the vacuum speed of light and $\varepsilon(\nu)$ the dielectric function. The light lines $\nu = v_{\mathrm{g}}q$ of the 800 nm ($v_{\mathrm{g,800}} = c_0/2.3$) and the 400 nm ($v_{\mathrm{g,400}} = c_0/3.03$) probe fields are also shown, where $v_{\mathrm{g}}$ and $q$ denote the group velocity and wave number, respectively. Phase-matching occurs at those frequencies for which the light lines intersect the phonon-polariton dispersion curve[18,34], that is, at 15 THz (PR), 16 THz (SH) and 19 THz (both PR and SH).

**Peak assignments in the PR amplitude spectrum.** Extended Data Fig. 5 displays a detailed assignment of all peaks in the amplitude spectrum of the PR measurement. Blue and red colours indicate up and down shifts, corresponding to sum and difference frequency mixing, respectively.

**Linear optical properties of $LiNbO_3$.** The low-frequency linear optical properties for light polarized along the $LiNbO_3$ $c$ axis are dominated by two optical phonon modes at 7.8 THz and 18.9 THz. They also include a weak mode at 8.2 THz and a feature at 21 THz which has been attributed to two-phonon absorption[11]. Extended Data Fig. 7 shows the terahertz reflectivity spectrum of the investigated sample, measured via Fourier transform infrared spectroscopy (FTIR), together with fits of four and two Lorentzian oscillators. The fit parameters for the two dominating optical phonons (listed in Extended Data Table 1) were used in the FDTD simulations of the phonon-polariton propagation. The reflectivity spectrum simulated from the parameters of these two oscillators agrees with the experimental data within the region of interest (12–20 THz).

**FDTD phonon-polariton simulations.** The phonon-polariton propagation dynamics in $LiNbO_3$ have been calculated by solving Maxwell's equations in space and time. To this end, we used FDTD in one spatial dimension[26].

We modelled the linear response of the material using the parameters of the two dominant optical phonons obtained from fitting the FTIR measurement (see above). For each mode, the equation of motion is given by

$$\ddot{Q}_{\mathrm{IR}} + 2\gamma\dot{Q}_{\mathrm{IR}} + \omega_{\mathrm{TO}}^2 Q_{\mathrm{IR}} = Z^* E(t)$$

Here, $\gamma$ is the damping constant, $\omega_{\mathrm{TO}}$ the phonon angular frequency and $Z^*$ the phonon-mode effective charge, which can be expressed as $\omega_{\mathrm{TO}}\sqrt{\varepsilon_0 - \varepsilon_\infty}\sqrt{\epsilon_0/n}$ with $n$ the oscillator density, $\epsilon_0$ the vacuum permittivity, and $\varepsilon_0$ and $\varepsilon_\infty$ the low-frequency and high-frequency limits of the dielectric function, respectively. The oscillator density was approximated as one oscillator per unit cell. For each mode, $\varepsilon_0$ and $\varepsilon_\infty$ were derived from the generalized Lyddane–Sachs–Teller relation[35].

The above equation was solved at every discrete point of the grid in space and time using the values of the electric field calculated from Maxwell's equation. The oscillator equation and Maxwell's equation are coupled via the electric displacement field

$$D = \epsilon_0\varepsilon_\infty E + \omega_{\mathrm{TO}}\sqrt{\varepsilon_0 - \varepsilon_\infty}\sqrt{\epsilon_0 n}\; Q_{\mathrm{IR}}$$

The linear optical properties of $LiNbO_3$ are well reproduced by our simulation (see Extended Data Fig. 7).

Nonlinear effects were captured by introducing the lattice anharmonicities of the driven $A_1$ mode into the above equation of motion:

$$\ddot{Q}_{\mathrm{IR}} + 2\gamma\dot{Q}_{\mathrm{IR}} + \omega_{\mathrm{TO}}^2 Q_{\mathrm{IR}} + a_3 Q_{\mathrm{IR}}^2 + a_4 Q_{\mathrm{IR}}^3 + a_5 Q_{\mathrm{IR}}^4 = Z^* E(t)$$

The anharmonic coefficients $a_3$, $a_4$ and $a_5$ are taken from *ab initio* DFT calculations as described below ($a_3 = 1{,}567.65\,\mathrm{meV\,amu^{-3/2}\,Å^{-3}}$, $a_4 = 900.8\,\mathrm{meV\,amu^{-2}\,Å^{-4}}$, $a_5 = 7.1\,\mathrm{meV\,amu^{-5/2}\,Å^{-5}}$). Here, the mid-infrared pump pulse was set to a field

strength of 30 MV cm$^{-1}$, carrier frequency 17.5 THz and duration 180 fs, comparable to the experiment.

We evaluated the equations in time steps of 0.5 fs and with a spatial grid of 0.5 μm. Perfectly matched boundary conditions were implemented to impede back reflection.

**DFT calculations for the potential energy along the $A_1$ coordinate.** To explore the nonlinear response of a resonantly excited phonon mode we performed first-principle computations within the framework of DFT. All our computations were carried out using DFT as implemented in the QUANTUM ESPRESSO code[36]. We used ultrasoft pseudopotentials, which contain as valence states the $2p2s$ for lithium, $4s^2 4p^6 4d^4 5s^1$ for niobium and $2s^2 2p^4$ for oxygen. As numerical parameters, we applied a cut-off energy of 80 Rydberg (Ry) for the plane-wave expansion and 400 Ry for the charge density. For all computations, we sampled the Brillouin zone with a $17 \times 17 \times 17$ $\boldsymbol{k}$-point mesh generated with the Monkhorst and Pack scheme[37] and reiterated total energy calculations until the total energy became less than $10^{-10}$ Ry. Before calculating phonon-modes, we fully structurally relaxed the unit cell regarding forces and pressure below the threshold of 5 μRy per $a_0$. We performed density functional perturbation theory[38] calculations to obtain phonon-mode eigenvectors and frequencies of the phonon modes. Finally, we computed the anharmonic phonon potential by calculating the total energy for structures, which have been modulated with the phonon eigenvector. Least-mean-square fits of this total energy landscape reveal the anharmonic coefficients of equation (2) of the main text and the phonon-mode eigenvector as shown in Fig. 1a.

**Scaling the reconstructed potential.** The unknown proportionality factor $B$, which connects the measured SH signal to the vibrational velocity via $I_{SH}(\tau) = B\dot{Q}(\tau)$, leaves a single scaling factor to the reconstruction. The kinetic energy becomes $E_{kin}(\tau) = [I_{SH}(\tau)/B]^2/2$ and the vibrational amplitude $Q(\tau) = \int [I_{SH}(\tau)/B] \mathrm{d}\tau$. Hence, the $y$ axis of the reconstruction will be scaled with $B^2$ and the $x$ axis with $B$ to the correct absolute values. This constant $B$ can be derived by fitting the function $f(Q) = (1/B^2)U(BQ)$ to the experimental data, where $U(Q)$ is the potential obtained by DFT. Once $B$ is retrieved, the experimental $x$ axis and $y$ axis can be rescaled to the absolute phonon amplitude in terms of Å amu$^{1/2}$ and the potential energy in eV, respectively.

The maximum displacement of the oxygen atoms involved in the $A_1$ vibrational mode was calculated with the knowledge of the phonon eigenvectors, which we obtained from DFT calculations. We find a maximum displacement of the oxygen atoms of approximately 14 picometres, which amounts to 7% of the Nb–O and 5% of the O–O nearest-neighbour distance at the corresponding potential energy (0.7 eV), which agrees with the estimated energy deposited per unit cell (0.6 eV at a pulse energy of 3 μJ).

**Effects of $g_j Q_{IR}^2 Q_j$ nonlinear phonon coupling.** As well as the anharmonicity of the driven lattice mode, the full lattice potential also comprises nonlinear coupling to other phonon modes of the form $g_j Q_{IR}^2 Q_j$:

$$U(Q_{IR}, Q_j) = \frac{1}{2}\omega_{TO}^2 Q_{IR}^2 + \frac{1}{3}a_3 Q_{IR}^3 + \frac{1}{4}a_4 Q_{IR}^4 + \frac{1}{5}a_5 Q_{IR}^5 + \sum_j \frac{1}{2}\omega_j^2 Q_j^2 + \sum_j g_j Q_{IR}^2 Q_j$$

Here, $Q_j$ denotes the amplitude of a coupled lattice mode and $\omega_j$ its resonance frequency[5,8,9]. For strongly driven $Q_{IR}$, the nonlinear interaction leads to a directional force on the coupled mode $Q_j$, which can be used to control the functionality of materials[8].

In addition, the finite amplitude $Q_j$ renormalizes the fundamental frequency of $Q_{IR}$, as can be seen in the equations of motion:

$$\ddot{Q}_{IR} + 2\gamma\dot{Q}_{IR} + (\omega_{TO}^2 - 2gQ_j)Q_{IR} = Z^* E(t)$$

$$\ddot{Q}_j + 2\gamma_j\dot{Q}_j + \omega_j^2 Q_j = g_j Q_{IR}^2$$

This frequency renormalization $\omega'_{TO} = \sqrt{(\omega_{TO}^2 - 2gQ_j)}$ was observed in our experiment with a maximum change of 3.5% at the highest driving field (see Extended Data Fig. 6).

**Data availability.** The data that support the findings of this study are available from the corresponding author on reasonable request.


30. Mlejnek, M., Wright, E. M., Moloney, J. V. & Bloembergen, N. Second harmonic generation of femtosecond pulses at the boundary of a nonlinear dielectric. *Phys. Rev. Lett.* **83,** 2934 (1999).
31. Wahlstrand, J. K., Merlin, R., Li, X., Cundiff, S. T. & Martinez, O. E. Impulsive stimulated Raman scattering: comparison between phase-sensitive and spectrally filtered techniques. *Opt. Lett.* **30,** 926 (2005).
32. Träger, F. *Springer Handbook of Lasers and Optics* (Springer, 2007).
33. Dharmadhikari, J. A., Dota, K., Mathur, D. & Dharmadhikari, A. K. Spectral broadening in lithium niobate in a self-diffraction geometry using ultrashort pulses. *Appl. Phys. B* **140,** 122–129 (2016).
34. Stevens, T., Wahlstrand, J. K. & Merlin, R. Cherenkov radiation at speeds below the light threshold: phonon-assisted phase matching. *Science* **291,** 627–630 (2001).
35. Chaves, A. S. & Porto, S. P. S. Generalized Lyddane–Sachs–Teller relation. *Solid State Commun.* **13,** 865–868 (1973).
36. Giannozzi, P. *et al.* QUANTUM ESPRESSO: a modular and open-source software project for quantum simulations of materials. *J. Phys. Condens. Matter* **21,** 395502 (2009).
37. Monkhorst, H. & Pack, J. Special points for Brillouin-zone integrations. *Phys. Rev. B* **13,** 5188 (1976).
38. Baroni, S., de Gironcoli, S., Dal Corso, A. & Giannozzi, P. Phonons and related crystal properties from density-functional perturbation theory. *Rev. Mod. Phys.* **73,** 515 (2001).

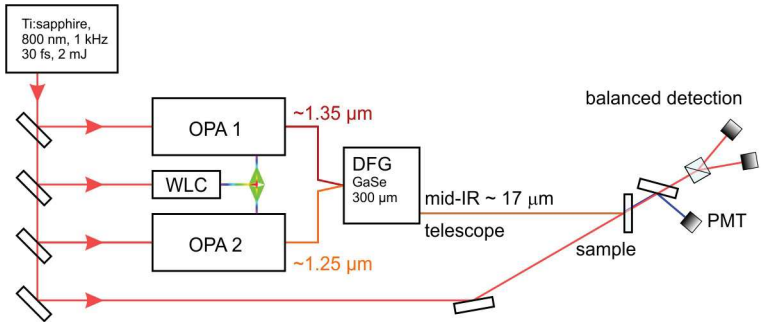


**Extended Data Figure 1 | Experimental set-up.** Pulses (30 fs) from a Ti:sapphire amplifier are used to pump two optical parametric amplifiers (OPA), which are seeded by the same white-light continuum (WLC). CEP-stable, 3 μJ, 150 fs pulses at 17 μm wavelength are obtained by difference frequency generation (DFG) of the two signal beams from the OPAs. The mid-infrared light is focused to a spot size of approximately 65 μm using a telescope and overlapped with the 800 nm probe beam (40 nJ, 35 μm spot size).

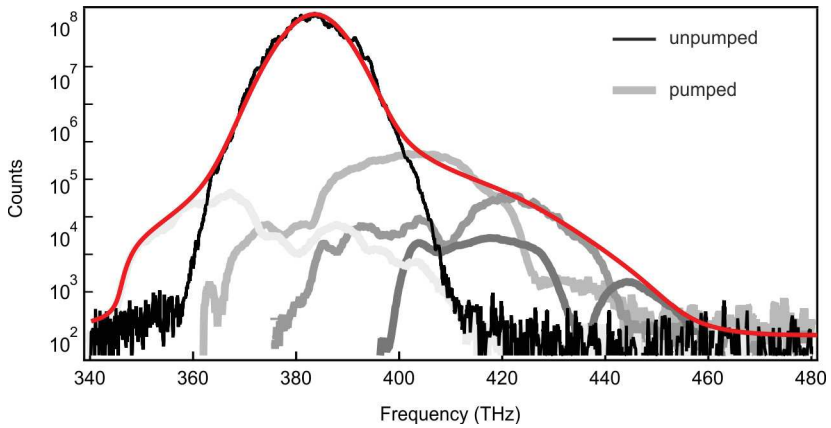


**Extended Data Figure 2 | Sideband generation from phonon harmonics.** The black solid line is the incident spectrum of the 800 nm probe pulses with a bandwidth of about 30 THz. The grey solid lines are the sidebands generated from the phonon harmonics measured at different positions behind the $LiNbO_3$ crystal. Owing to momentum conservation, each sideband propagates in a slightly different direction compared with the unperturbed 800 nm beam. The red line is a guide to the eye of the resulting spectral broadening.

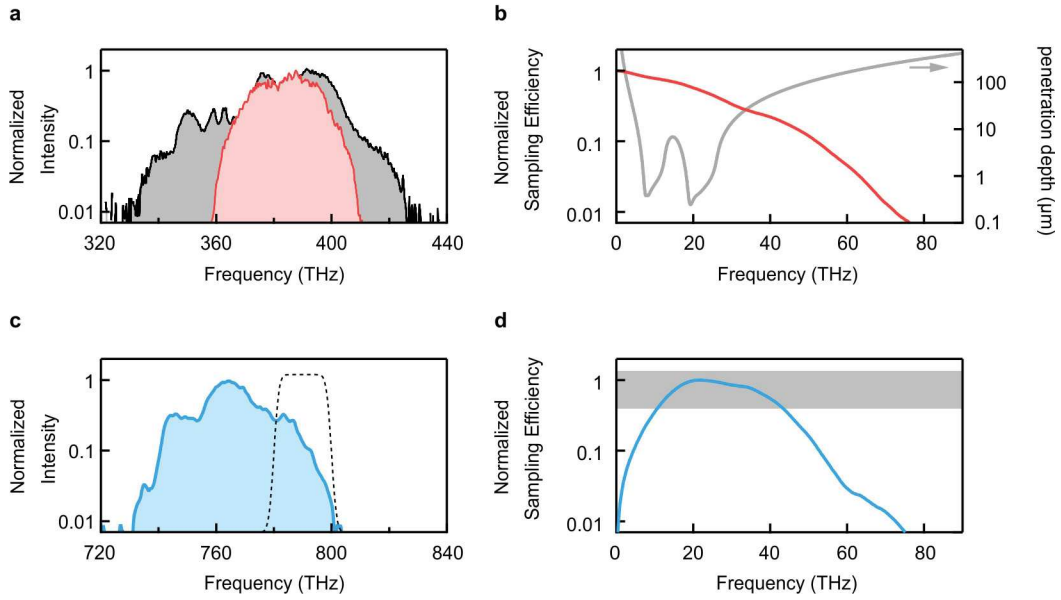


**Extended Data Figure 3 | Probe spectra and sampling efficiencies.** **a**, Spectrum of the 800 nm probe pulse before (red) and after (grey) propagation through the unpumped $LiNbO_3$ crystal in units of THz. **b**, Red curve: sampling efficiency of the 800 nm light calculated with the spectrum shown in **a**. The grey curve is the penetration depth in the mid-infrared region obtained from FTIR spectroscopy. **c**, Spectrum of the generated SH light (blue curve) and normalized transmission of the bandpass filter placed in front of the detector (dashed curve), also shown in units of THz. **d**, Sampling efficiency of the SH light with the spectrum shown in **c**. The sampling efficiency is almost constant in the 15–45 THz region of the first three phonon harmonics.

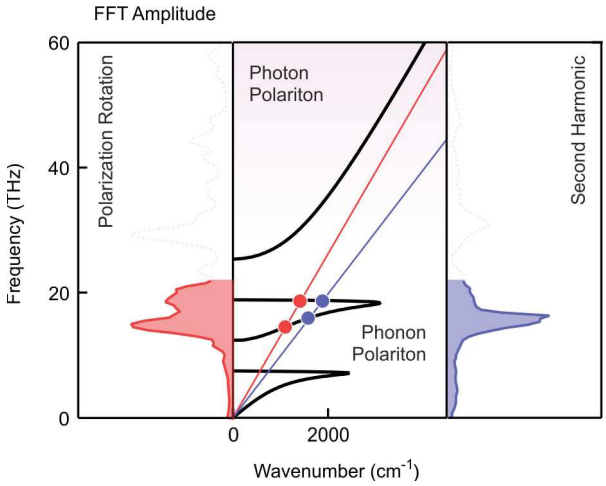


**Extended Data Figure 4 | Phonon-polariton dispersion.** The phonon-polariton dispersion of the two dominant lattice modes in $LiNbO_3$ (black curve) and two light lines $\nu = v_g q$ for 800 nm (red) and 400 nm (blue) wavelengths are shown. The dots mark the points of intersection with the dispersion relation, which correspond to the observed fundamental frequencies of the driven mode (left and right panels).

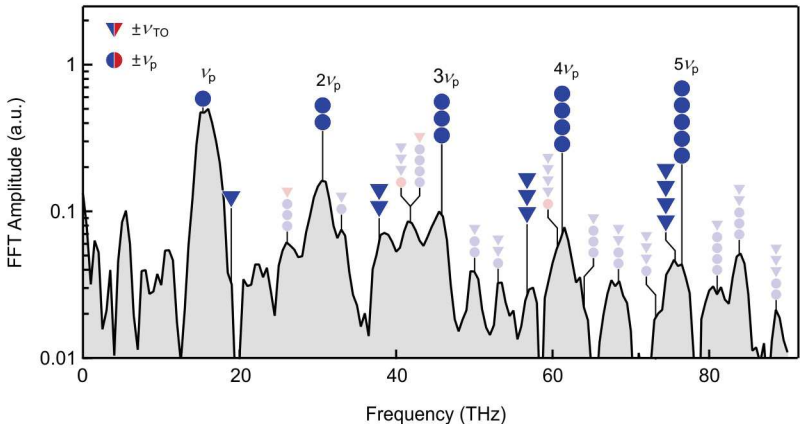


**Extended Data Figure 5 | Assignment of phonon harmonics.** The amplitude spectrum of the time-resolved PR measurement is shown. Blue symbols denote a blueshift of 15 THz (triangles) and 19 THz (circles). Multiple symbols represent shifts by multiples of the corresponding frequencies. Red symbols denote redshifts.

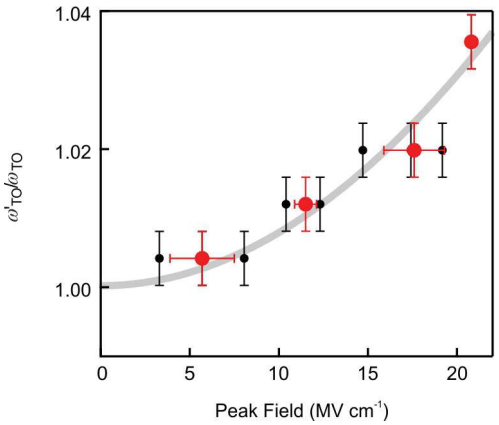


**Extended Data Figure 6 | Phonon frequency renormalization.** The black circles denote the peak-field-dependent fundamental phonon frequencies extracted from Fourier transformations of the time-resolved signals. Values at the same frequency have been binned (red circles) to account for the limited frequency resolution of the FFT analysis. The error bars denote $1\sigma$ (67% confidence interval). The grey line is a fit to the data with the function $f(E) = \sqrt{1 + aE^2}$.

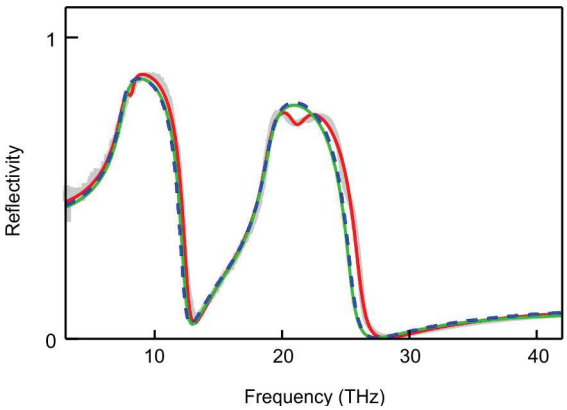


**Extended Data Figure 7 | Terahertz reflectivity spectrum.** The grey solid line is the measured terahertz reflectivity spectrum of $LiNbO_3$ with light polarized along the *c* axis. The red line is a fit considering four Lorentzian oscillators. The dashed blue line is a fit considering only the two dominant phonon modes at 7.5 THz and 19 THz. The green line is the FDTD simulated reflectivity when only these two oscillators are considered (see Methods).

**Extended Data Table 1 | Parameters for the $A_1$ Lorentzian oscillator**

| Oscillator # | Frequency ($cm^{-1}$) | Oscillator strength ( $cm^{-1}$) $\omega_{TO}\sqrt{\varepsilon_0 - \varepsilon_\infty}$ | Damping ( $cm^{-1}$) |
|---|---|---|---|
| 1 | 249.3 | 922.8 | 27.7 |
| 2 | 271.6 | 384.1 | 20 |
| 3 | 632 | 955.9 | 33.5 |
| 4 | 696.7 | 352.5 | 76.2 |
| $\varepsilon_\infty$ | 4.4054 | | |

Frequencies, oscillator strengths and damping constants of the $LiNbO_3$ vibrational modes were obtained from a fit of four Lorentzian oscillators to the reflectivity spectrum.